Nanostructured Pseudocapacitors Based on Atomic Layer Deposition of V_2O_5 onto Conductive Nanocrystal-based Mesoporous ITO Scaffolds

Iris E. Rauda, Veronica Augustyn, Laura C. Saldarriaga-Lopez, Xinyi Chen, Laura T. Schelhas, Gary W. Rubloff, Bruce Dunn,* and Sarah H. Tolbert**

Solution processing of colloidal nanocrystals into porous architectures using block co-polymer templating offers a simple yet robust route to construct materials with open porosity and high surface area. These features, when realized in materials that show efficient redox activity and good conductivity, should be ideal for electrochemical energy storage because they allow for efficient electrolyte diffusion and ample surface and near-surface redox reactions. Here, a route to synthesize nanoporous pseudocapacitors is presented using preformed ITO nanocrystals to make a conductive scaffold, coated with a conformal layer of vanadia deposited using atomic layer deposition (ALD). Two vanadia thicknesses are deposited, 2 and 7 nm, to examine the kinetics of Li^+ diffusion into vanadia in a system where all other chemical and structural parameters are fixed. Porosity measurements show that the internal surface area of 2 nm vanadia samples is fully accessible; whereas for the 7 nm vanadia, there is some pore blockage that limits electrolyte diffusion. Despite this fact, composites with both thick and thin vanadia layers show high levels of pseudocapacitance, indicating fast diffusion of Li^+ through even the 7 nm thick vanadia. This work thus sets a minimum accessible length-scale of 7 nm for intercalation pseudocapacitance in orthorhombic V_2O_5.

1. Introduction

Electrochemical energy storage devices known as pseudocapacitors have attracted much attention because they have the ability to attain high energy densities while maintaining high power densities.[1] Pseudocapacitors store charge through fast and reversible faradaic processes that involve surface or near-surface redox reactions. These charge storage mechanisms are different than those in traditional batteries because they are not limited by the diffusion of ions into the bulk material. Therefore, pseudocapacitors can offer several benefits when compared to batteries including fast charge/discharging within seconds, good charge/discharge cycling stability, and the ability to deliver >10× more power.[2] An ideal pseudocapacitor electrode architecture should comprise a redox-active material (e.g., a metal oxide) that has a nanodimensional structure to accommodate shorter ion diffusion lengths. In addition, the material should have a high surface area in order to maximize electrolyte accessible redox-active sites, and, have an open interconnected porosity to facilitate solvent diffusion to all of these redox-active sites. Finally, electrical conductivity should be integrated and wired into the redox-active component in order to simultaneously achieve both higher energy and power densities in one structure.

The improvements to electrochemical energy storage resulting from building electrical conductivity into electrode materials are well established in the literature. Carbon-based materials such as carbon nanotubes (CNT) and graphene have been shown to act as good conductive platforms for the construction of composite electrodes. For example, CNT-based composites of manganese oxide (MnO_2),[3] titanium oxide (TiO_2),[4] tin oxide (SnO_2),[4] lithium manganese oxide ($LiMn_2O_4$),[5] and V_2O_5[6–10] have been reported. Graphene-based composites of $LiMn_2O_4$,[5] iron oxide (Fe_3O_4),[11] SnO_2,[12] $Ni(OH)_2$,[13] and MnO_2[14] have also been produced as well as other carbon scaffolds with interesting architectures.[15,16] In addition to carbon-based conductors, metals have also been integrated into composite electrodes with unique architectures including an interpenetrated nickel inverse opal,[17] nanoporous gold,[18] nickel porous foams,[19,20] copper pillar arrays,[21] and stainless steel meshes.[22] In the examples above, the conductive component provided a network for good electrical transport

Dr. I. E. Rauda, Dr. L. C. Saldarriaga-Lopez, Dr. L. T. Schelhas, Prof. S. H. Tolbert
Department of Chemistry and Biochemistry, UCLA
Los Angeles, CA 90095–1569, USA
E-mail: tolbert@chem.ucla.edu
Dr. V. Augustyn, Prof. B. Dunn, Prof. S. H. Tolbert
Department of Materials Science & Engineering, UCLA
Los Angeles, CA, 90095, USA
E-mail: bdunn@ucla.edu
Dr. X. Chen,[+] Prof. G. W. Rubloff
Department of Materials Science & Engineering
University of Maryland
College Park, MD 20742, USA
E-mail: rubloff@umd.edu
Prof. B. Dunn, Prof. S. H. Tolbert
The California NanoSystems Institute, UCLA
Los Angeles, CA, USA
[+]Present address: Lam Research, 11155 SW Leveton Dr. Tualatin, OR 97062

DOI: 10.1002/adfm.201401284

throughout the active material which resulted in improvements to the electrochemical performance.

Electrical conductivity is important for enabling the charge transfer which leads to faradaic reactions in pseudocapacitor materials, but that in itself is not enough to convert a standard intercalation based battery material into a pseudocapacitive material. In addition, a high interfacial area in contact with the electrolyte is also necessary. For example, we reported significant enhancements to the capacitive charge storage behavior in nanocrystal-based mesoporous TiO_2 pseudocapacitors templated using poly(ethylene oxide-*block*-hydrocarbon) [PEO-XXX] type polymers.[23] In that work, the porous titania architectures demonstrated high levels of pseudocapacitive charge storage that were accompanied by rapid charging/discharging rates.[23] The improved performance resulted from the unique architecture, which exhibited an open interconnected porosity that facilitated rapid solvent diffusion throughout the material, as well as a high density of redox-active surface sites arising from the nanocrystals within the pore walls. Bein and coworkers have also reported the preparation of mesoporous films from TiO_2 nanocrystalline particles that demonstrated high Li insertion capacities and fast charging rates resulting from the high surface to bulk ratio of the nanocrystals and the easily accessible mesoporous structures.[24] The literature includes a variety of other examples of this type of polymer templated nanocrystal-based co-assembly to prepare porous architectures.[25–28]

More recently, we have developed a general route for assembling pre-formed ligand-stripped[29] nanocrystals into hierarchical mesoporous architectures,[30] and it is those chemistries that are used in this work. Model redox-active systems included Mn_3O_4, $(Mn,Fe)_2O_3$, and tin-doped indium oxide (ITO), and similar to our TiO_2 nanocrystal-based materials,[23] we found that templated Mn_3O_4 nanocrystal-based films exhibited enhanced charge storage behavior compared to untemplated nanocrystals, again demonstrating the efficacy of a nanocrystal based nanoporous electrode architecture.[30] Moreover, we demonstrated high synthetic tunability where the mesoporosity could be tuned by varying the polymer template, and the microporosity could be tuned by varying the size of the nanocrystal.[30] We also established that the method could be applied to non-oxide systems.[31] Other recent studies showed that this method also works with polymers containing non-PEO polar blocks.[32]

While our polymer templated nanocrystal-based mesoporous materials provide an attractive and effective electrode architecture, they will ultimately be limited by electrical conductivity when scaled up to prepare thick electrodes. Therefore, in order to build electrodes with more ideal architectures, we need to integrate a conductor into our materials while still retaining the high surface area and open interconnected porosity. Here, we use solution-phase methods to construct porous conductive scaffolds by templating ITO nanocrystals into mesoporous architectures and subsequently coating the ITO with V_2O_5 via atomic layer deposition (ALD) to produce pseudocapacitor electrode composites. The Rubloff group recently developed and optimized a new ALD V_2O_5 process that resulted in highly conformal and crystalline V_2O_5 films that demonstrated high performance electrochemical energy storage.[10,33,34] We use this process to coat porous ITO with two different thicknesses: 2 nm and 7 nm V_2O_5 layers. We also study crystallinity effects in the V_2O_5 layers by heating to various temperatures and examine the pseudocapacitive response.

In addition to our examination of model pseudocapacitor architectures, this work allows us to explore some fundamental questions related to pseduocapacative charge storage. For example, by using two different vanadia film thicknesses, this unique system allows us to explore the kinetics of Li^+ motion into vanadia layers of different thicknesses. Specifically, we try to answer the question—how thick can a vanadia film be before the charge storage has a significant non-capacitive contribution? The answer should have significant ramifications in the rational design of nanoscale pseudocapacitors.

2. Results and Discussion

2.1. Synthesis of ITO-V_2O_5 Composites

We previously reported the synthesis of mesoporous ITO nanocrystal-based films.[30] Here, we use poly(ethylene-*alt*-propylene)-*block*-poly(ethylene oxide), (PEP-*b*-PEO) as the block copolymer template. ITO nanocrystals capped with amine functional ligands were synthesized according to literature procedures.[35,36] Next, the as-synthesized nanocrystals were stripped of their ligands using an $NOBF_4$ treatment to produce bare nanocrystals that were charge-stabilized.[26] **Figure 1**b shows a

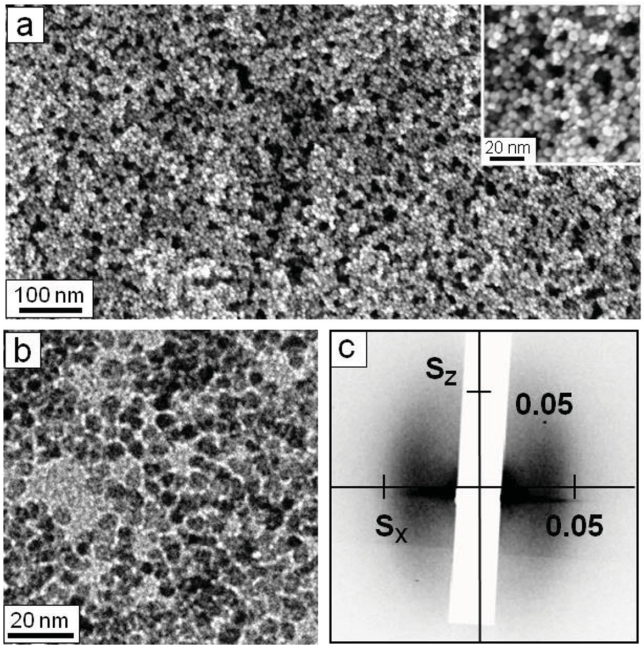

Figure 1. a) Low-magnification SEM image of a templated ITO nanocrystal-based mesoporous film. Inset: higher-magnification image showing pore walls comprising individual ITO nanocrystals. b) TEM image of ligand-stripped ITO nanocrystals with an average diameter of 4.6 ± 0.4 nm. c) 2D-SAXS pattern obtained on a ITO nanocrystal-based porous film, collected at an angle of incidence $\beta = 1.25°$. The pattern shows strong in-plane scattering, indicative of a well-defined pore size, but no long range periodicity of the pores. Scattering vector *S* components are given in 1/nm.

TEM image of ligand-stripped ITO nanocrystals with an average diameter of 4.6 ± 0.4 nm demonstrating they are uniform in shape and size, and free of agglomeration. Ligand-stripped ITO nanocrystals, dispersed in ethanol with ≈10% dimethylformamide (DMF) (v/v), were mixed with PEP-*b*-PEO, dissolved in pure ethanol, to prepare the coating solution. Thin-films were then either dip-coated or spin-coated onto clean polar substrates through an evaporation-induced self-assembly process.[37] In solution, the polymer self-assembles to form micelles and, upon evaporation of the solvent, the ITO nanocrystals associate with the polar PEO block to yield a mesostructured organic/inorganic composite. The polymer template was then thermally decomposed by heating the films to 450 °C, resulting in ITO nanocrystal-based mesoporous architectures.

Figure 1a shows a low-magnification SEM image of a mesoporous ITO film exhibiting a bimodal porosity with a combination of mesopores, created by the polymer template, and micropores which arise from the spaces between the nanocrystals that make up the pore walls. The mesopores, with an average pore size of 15 ± 3 nm, are locally disordered; however, they do retain a macroscopically homogeneous porosity. The films are crack-free and maintain open porosity at the surface. A closer look at a high-magnification image (inset of Figure 1a) shows individual ITO nanocrystals that comprise the pore walls, which are approximately 1–3 nanocrystals thick. Because the nanocrystals do not completely fuse to form a dense wall, the voids between them give rise to micropores that significantly increase the surface area of the material.

To further characterize the nanoscale architecture we performed two-dimensional small-angle X-ray scattering (2D-SAXS) and ellipsometric porosimetry measurements. Figure 1c shows the 2D-SAXS pattern obtained for mesoporous ITO films, collected at an angle of incidence $\beta = 1.25°$. The pattern shows a diffuse ellipsoidal ring with strong in-plane scattering, indicative of a homogenous but non-periodic pore structure with a characteristic pore + wall distance of 32 nm. The porosity of the ITO films was analyzed by ellipsometric porosimetry using toluene as the adsorbate.[38] **Figure 2**a shows an adsorption-desorption isotherm for a mesoporous ITO film that exhibits typical type IV behavior.[39] The hysteresis present at higher relative pressures is indicative of a mesostructured material with an open interconnected porosity. The adsorption and desorption curves describe the cage and neck sizes of the mesopores. A Kelvin model fit to the isotherm produces pore size distributions for the cages centered at 25 nm, and for the necks at 11 nm, as shown in Figure 2b. The data confirm that the template nanocrystal based ITO films exhibit bimodal porosity that leads to high surface area combined with interconnected, open porosity. The isotherm in Figure 2a shows a 53% toluene-accessible pore volume. It should be noted that the average mesopore sizes found by porosimetry (Figure 2a–b) agree with lengthscales determined by 2D-SAXS (Figure 1c) and SEM (Figure 1a). In addition, the pore size can be varied by changing the polymer to nanocrystal ratio, thus allowing many different pore sizes to be produced. In this work, ITO frameworks with pore sizes varying from about 15 nm to about 25 nm were used.

The ITO films discussed below function as high surface area, porous, conductive scaffolds. Once prepared, we coated the ITO scaffolds with thin film layers of V_2O_5 via an ALD process.[33] ALD is a low temperature thin film growth technique where the surface to be coated is sequentially exposed to various precursors, leading to predictable monolayer growth with superb uniformity even over demanding topography, such as high-aspect ratio nanostructures.[40,41] In this process, we explored two ALD processes using different oxidants- water and ozone. We also studied two different thicknesses, ≈2 nm and ≈7 nm V_2O_5 layers, where the thickness is controlled by the number of ALD cycles (see experimental details). The composites were then annealed using rapid thermal annealing (RTA) in air at various temperatures allowing us to study the effects of crystallinity in the V_2O_5 layers. X-ray photoelectron spectroscopy (XPS) measurements (Figure S1, Supporting Information) confirmed that heated samples contained pre-dominantly penta-valent vanadium, with 91% of vanadium atoms in the 5+ valence state and 9% in the 4+ valence state for 2 nm layers, and 96% in the 5+ valence state and 4% in the 4+ valence state for 7 nm layers. The observed binding energies for V^{5+} and V^{4+} were also found to be in agreement with literature values,[42] and the trends with film thickness indicate that the small amount of the V^{4+} was probably at the surface of the thin ALD films.

2.2. Structure and Electrochemical Properties of 2 nm V_2O_5 Layers

Figure 3a–c shows top-view SEM images of smaller pore ITO films that were coated with a 2 nm layer of V_2O_5 (ozone-based, 100 ALD cycles) as-deposited (Figure 3a), heated to 200 °C (Figure 3b), and heated to 450 °C (Figure 3c). All three composites feature open porosity with visible mesopores with average diameters of 18 ± 3 nm (Figure 3a), 16 ± 3 nm (Figure 3b), and 15 ± 3 nm (Figure 3c). These values are all basically equivalent, given the statistical error, and are in agreement with the average diameter of 15 ± 3 nm determined for uncoated mesoporous ITO (Figure 1a). Importantly, in the higher-magnification images (insets) of Figure 3a–c, the presence of individually coated nanocrystals is visible, demonstrating that this process produces conformal vanadia layers around the ITO scaffold. Closer examination indicates that there is some grain growth of the V_2O_5 around the nanocrystals in the layers heated to 200 °C, while the layers heated 450 °C show clear grain growth. These results illustrate one of the challenges of this synthetic method, which is that V_2O_5 crystallization and coarsening are coupled processes and one cannot induce one without the other. As a result, we expect samples crystallized at higher temperatures to show smaller mesopore pore size and some filling of the micropores.

We used ellipsometric porosimetry to analyze the porosity of the composites after coating, focusing first on a large pore ITO with a 2 nm thick V_2O_5 coating. For this sample, the uncoated porous ITO film showed a pore size distribution for the cages centered at 25 nm, and for the necks at 11 nm, (Figure 2b). The total pore volume is 53%. Adsorption-desorption isotherms for vanadia coated films heated to 200 °C (Figure 2c) and 450 °C (Figure S2c, Supporting Information) show typical type IV behavior with hysteresis at higher relative pressures suggesting the composites are mesoporous with open interconnected

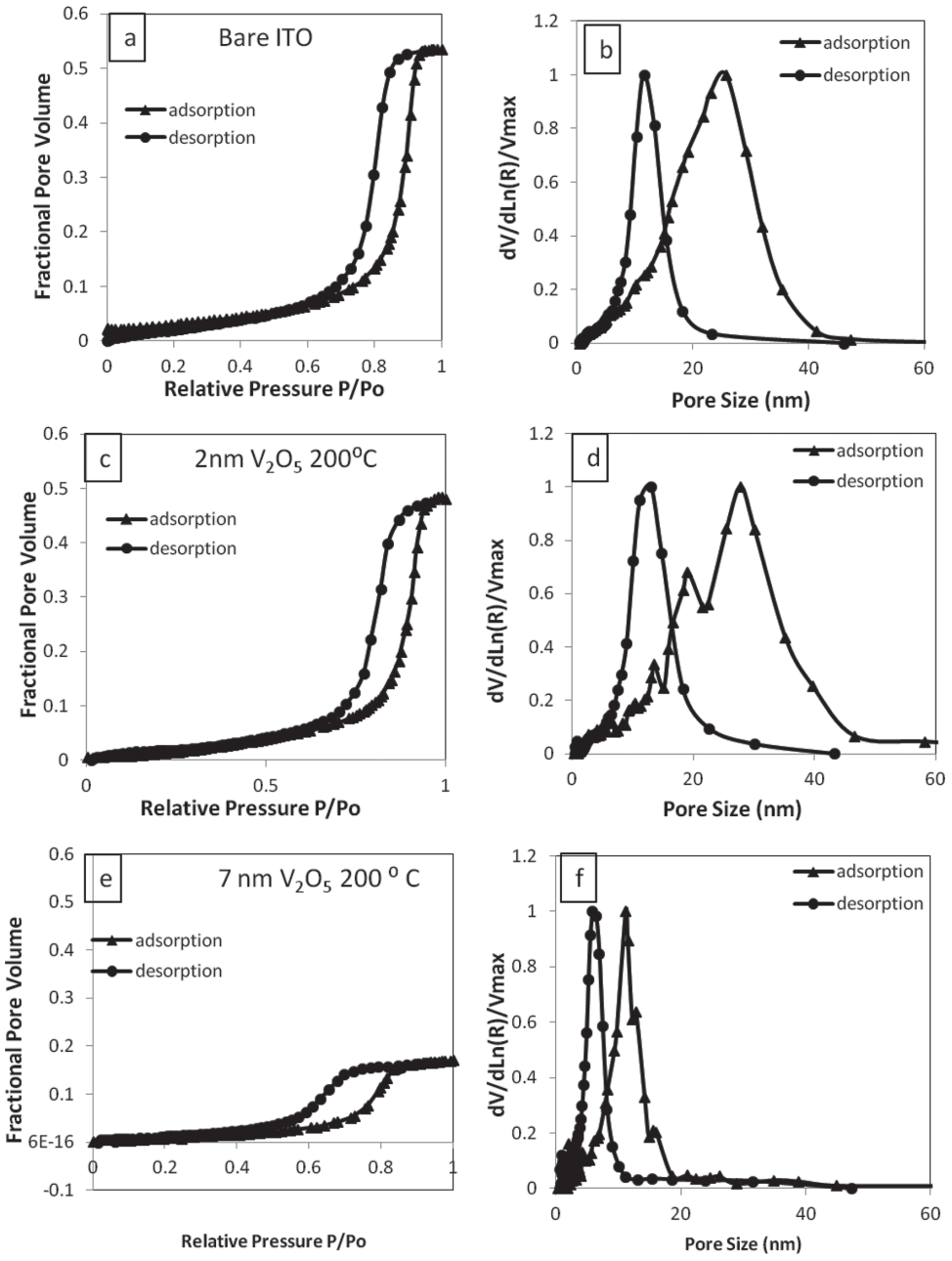

Figure 2. Toluene adsorption-desorption isotherms showing characteristic mesoporous behavior for a) a mesoporous ITO nanocrystal-based film, c) mesoporous ITO film coated with a 2 nm layer of V_2O_5 heated to 200 °C, e) mesoporous ITO film coated with a 7 nm layer of V_2O_5 heated to 200 °C. Pore size distribution data obtained from the isotherms for b) a mesoporous ITO nanocrystal-based film, d) mesoporous ITO film coated with a 2 nm layer of V_2O_5 heated to 200 °C, f) mesoporous ITO film coated with a 7 nm layer of V_2O_5 heated to 200 °C.

porosity. The total pore volume for the sample heated to 200 °C is 48% and is 43% for the sample heated to 450 °C. A Kelvin model fit to the isotherms produces pore size distributions centered around 26 nm (cage) and 13 nm (neck) for films heated to 200 °C (Figure 2d), and 23 nm (cage) and 12 nm (neck) for films heated to 450 °C (Figure S2c, Supporting Information). Mesopore size is thus similar to the bare ITO film for both samples suggesting that 2nm of V_2O_5 does not significantly perturb the pore structure in either film. **Table 1** summarizes porosimetry data for thin films heated to 200, 350, and 450 °C. For all thin films, the toluene-accessible pore volume is lower than the pore volume observed for the parent, uncoated ITO.

Cyclic voltammetry (CV) was performed to examine the charge storage behavior of the 2 nm V_2O_5 layers. The Li^+ insertion process can be expressed by $V_2O_5 + xLi^+ + xe^- \leftrightarrow Li_xV_2O_5$, where x represents the mole fraction of inserted lithium ions.[43] **Figure 4**a compares the charge storage dependence of 2 nm V_2O_5 heated to 200, 350 and 450 °C at sweep rates in the range between 2 mV/s to 100 mV/s. In all curves, the capacity increases with decreasing sweep rate, indicating that

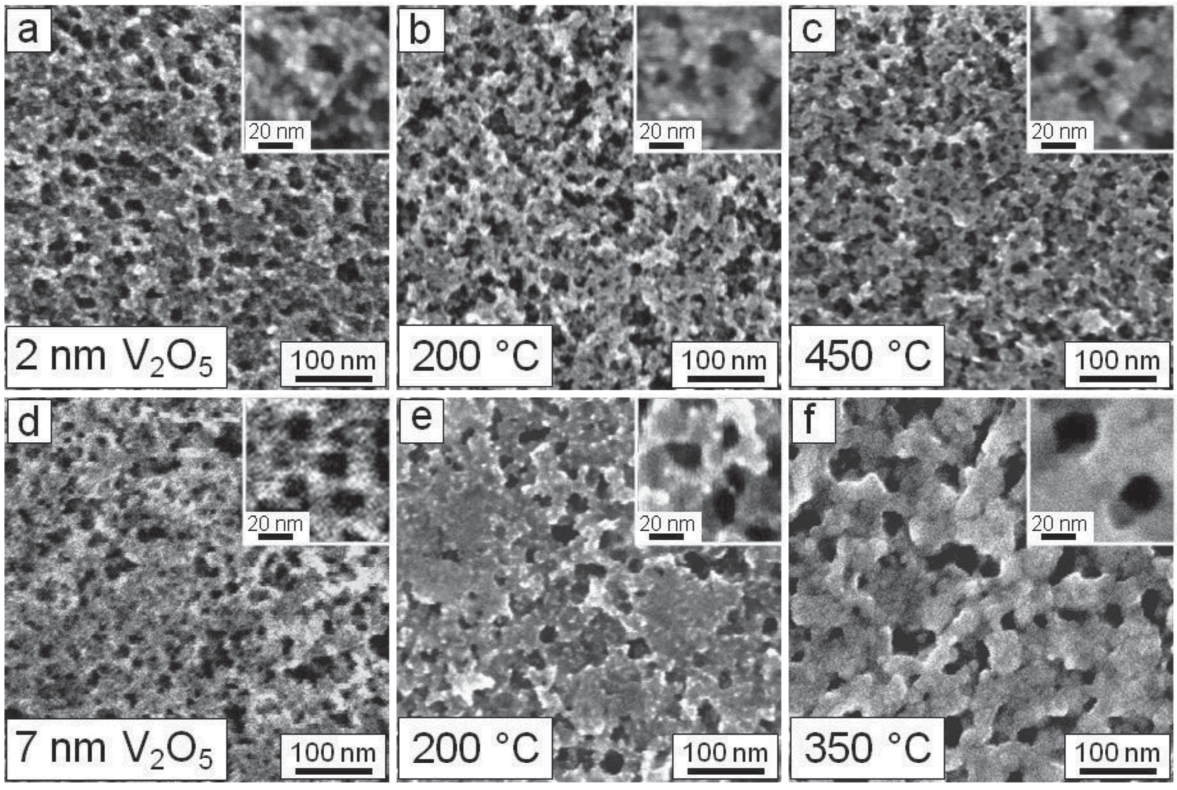

Figure 3. a–c) Low-magnification SEM images of mesoporous ITO films coated with a 2 nm layer of V_2O_5 as-deposited (a) (inset: higher-magnification image showing individually coated nanocrystals); heated to 200 °C (b) (inset: higher-magnification image showing grain growth of the V_2O_5 around the nanocrystals); and, heated to 450 °C (c) (inset: higher-magnification image showing grain growth of the V_2O_5 around the nanocrystals). d–f) Low-magnification SEM images of mesoporous ITO films coated with a 7 nm layer of V_2O_5 as-deposited (d) (inset: higher-magnification image showing spaces in between nanocrystals are filled in with V_2O_5); heated to 200 °C (e) (inset: higher-magnification image showing grain growth of V_2O_5 leads to partially fused pores); and, heated to 350 °C (f) (inset: higher-magnification image showing grain growth of the V_2O_5 leads to significant loss of mesostructure).

full storage has not been reached at the fastest rates. The V_2O_5 layer heated to 200 °C stores almost twice as much charge as the 2 nm layer heated to 450 °C. Figure 4b shows the charge storage dependence of 2 nm V_2O_5 heated to 200, 350, and 450 °C plotted as capacity versus charging time, as calculated from the various sweep rates in Figure 4a using a 2.2 V potential window. In this type of plot, the slow sweep rate behavior is more apparent and the region of mostly constant capacity after 440 sec indicates that the material is fully charged at this timescale. After a charging time of 200 s, the total charge stored for 200 °C treated samples is 1400 C/g, almost twice the amount of charge stored in samples heated to 450 °C. The trend is not linear with temperature, however, as samples heated to 350 °C show a capacity of 1200 C/g. While the majority of charge is stored in only 200 s, there is a measureable increase in capacity going to longer times, indicating that not all redox sites are kinetically accessible.

Table 1. Ellipsometric porosimetry data summarizing percent porosity, pore size, and neck size for thin 2 nm V_2O_5 films heated to 200 °C, 350 °C and 400 °C and for thick V_2O_5 films heated to 200 °C and 350 °C compared to their respective bare ITO film.

	Percent porosity	Cage Size [nm]	Neck Size [nm]
Bare ITO	53%	25	11
2 nm V_2O_5 200 °C	48%	26	13
Bare ITO	60%	22	13
2nm V_2O_5 350 °C	45%	23	12
Bare ITO	52%	25	11
2nm V_2O_5 450 °C	43%	23	12
Bare ITO	57%	22	11
7nm V_2O_5 200 °C	17%	12	6
Bare ITO	56%	22	11
7nm V_2O_5 350 °C	6%	12	7

In Figure 4, the differences in the gravimetrically normalized capacity observed between films heated to 200 and 350 °C can be attributed to the loss of porosity, as shown in Table 1. There is likely a small amount of grain growth that clogs a fraction of the smaller pores and leads to a lower total pore volume that can be accessible to the electrolyte. The difference in the capacity observed between films heated to 200 and 450 °C is likely explained by the atomic structure and bonding of the V_2O_5 layer. At 200 °C, the V_2O_5 should have a structure related to the orthorhombic phase, which is known to show facile Li^+ intercalation.[44] The material should also be less ordered, which

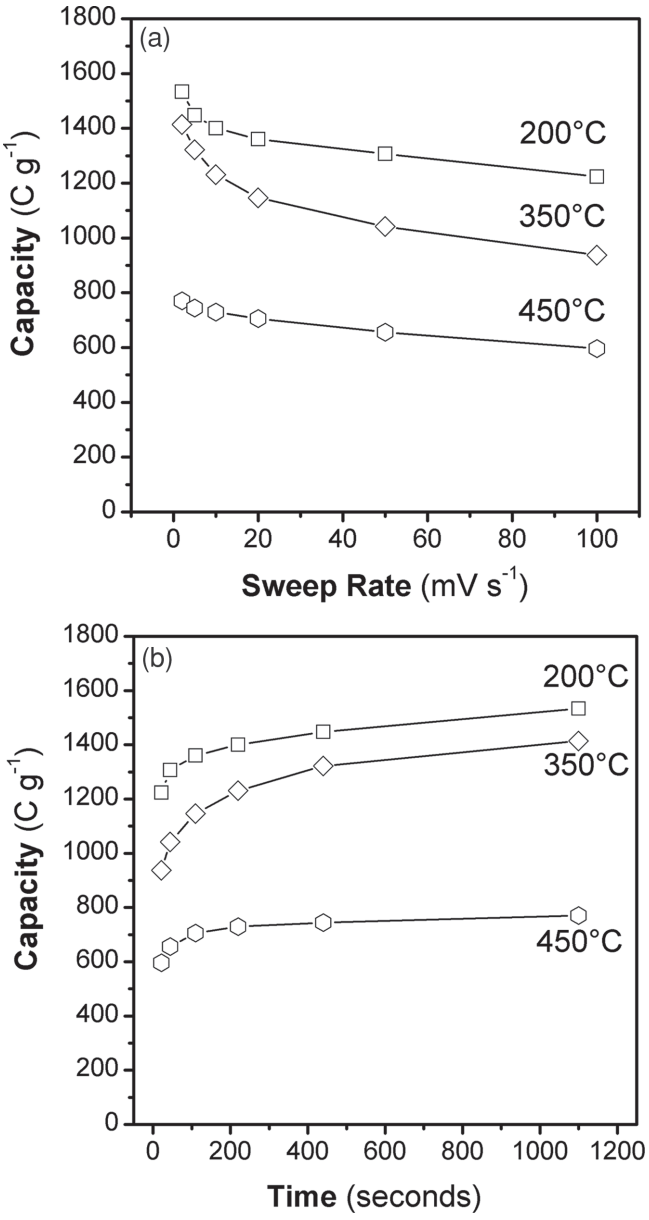

Figure 4. a) Charge storage dependence on sweep rate for mesoporous ITO films coated with a 2 nm layer of V_2O_5 heated to 200, 350, and 450 °C. b) Comparison of charging rates calculated from cyclic voltammetric data at various sweep rates for mesoporous ITO films coated with a 2 nm layer of V_2O_5 heated to 200, 350, and 450 °C.

can also increase redox sites.[44] When V_2O_5 is heated to 450 °C, a phase transition to the monoclinic crystalline structure occurs in bulk samples, leading to a reduction in Li^+ intercalation sites.[45] While redox pseudocapacitance is generally assumed to be a surface phenomenon, this data suggest that near-surface intercalation sites also contribute to redox pseudocapacitance and the lack of those near surface sites can cause a dramatic decrease in capacity.

We also investigated the effects of using different oxidants during the ALD process by comparing both water- and ozone-based 2 nm V_2O_5 coatings. Figure S4a (Supporting Information) compares the charge storage behavior in 2 nm V_2O_5 coated ITO synthesized with water and ozone and heated to 200 °C, cycled at sweep rates ranging from 1 mV/s to 100 mV/s. For both water- and ozone-based 2 nm V_2O_5 the capacity increases with decreasing sweep rate. Figure S4b shows the charge storage dependence plotted as capacity versus charging time. The trend we observe is that while the V_2O_5 films produced by both methods are similar, the ozone-based materials exhibit somewhat higher charge storage capacity than water-based V_2O_5. This result is consistent with our recent study of ozone-based and water-based V_2O_5 applied to Li-ion battery cathodes.[34] Previous work on ALD V_2O_5 films also suggested that residual carbon in the water-based vanadia could be partly responsible for the small differences in capacity.[33] XPS data collected on these materials (Figure S4c, Supporting Information), however, shows very low and very similar residual carbon contents for samples made using both methods. The XPS data in Figure S4c (Supporting Information) thus reconfirms the purity of the ALD deposited vanadia used here. It also indicates that the fast redox reactions observed in these materials are intrinsic to the conductive nanoscale composites produced here and are not caused by residual carbon.

2.3. Structure and Electrochemical Properties of 7 nm V_2O_5 Layers

We also investigated the effects of a thicker (7nm) V_2O_5 layer. Figure 3d–f shows top-view SEM images of porous ITO films that were coated with a 7 nm layer of V_2O_5 (ozone-based, 250 ALD cycles) as-deposited (Figure 3d), heated to 200 °C (Figure 3e), and heated to 350 °C (Figure 3f). Figure 3d shows that the thicker V_2O_5 fills most of the micropores but leaves most of the mesopores open. When the V_2O_5 layer is heated to 200 °C, as shown in Figure 3e, individual nanocrystals can no longer be seen, indicating that all of the micropores are filled, and V_2O_5 grain growth appears to block some of the mesopores as well. In Figure 3f one sees that when the V_2O_5 is heated to 350 °C, significant grain growth of the V_2O_5 leads to significant loss of mesostructure and many of the pores are clogged. The 7 nm V_2O_5 layers thus appear to be too thick to maintain the ideal porosity of these materials and so capacity loss due to pore blockage is expected in these materials. Despite this fact, kinetic studies on samples with thicker vanadia films should still provide insight about the rate of lithium insertion into the thick layers. We also note that because so much grain growth was observed by 350 °C, we did not attempt to anneal the thick film samples to 450 °C to examine the effects of the phase transition from orthorhombic to monoclinic; we felt that it would not be possible to separate the effects of the phase transition from the effects of grain growth.

Ellipsometric porosimetry measurements were also performed on the 7 nm V_2O_5 composites by using toluene as the adsorbate. Adsorption-desorption isotherms for films heated to 200 °C (Figure 2e) and 350 °C (Figure S2e, Supporting Information) show typical type IV behavior with a hysteresis at higher relative pressures indicating the films are mesoporous. A Kelvin model fit to the isotherms produces pore size distributions centered around 12 nm (cage) and 6 nm (neck) for films heated to 200 °C (Figure 2f), and 12 nm (cage) 7 nm (neck)

for films heated to 350 °C (Figure S2f, Supporting Information). The overall decrease in mesopore size is consistent with a thick layer of V_2O_5 coated ITO. The isotherms in Figure 2e and Figure S2e, also summarized in Table 1, show ≈17% and ≈6% toluene-accessible pore volume, respectively, which is lower than the pore volume calculated for uncoated ITO (56%, Figure S2a, Supporting Information) and 2 nm V_2O_5 coated ITO (48%, Figure 2c), also consistent with the fact that the ITO has been coated with a thicker layer of V_2O_5.

The charge storage behavior of the 7 nm V_2O_5 layers was also studied by CV. **Figure 5**a compares the charge storage dependence of 7 nm V_2O_5 heated to various temperatures (200, 250, 300, and 350 °C) at sweep rates ranging from 1–100 mV/s. As with the thinner films, for all temperatures, the gravimetrically normalized capacity increases with decreasing sweep rate, suggesting the V_2O_5 layer is not fully charged because of slow diffusion of Li+ ions into the structure, even at the slowest sweep rates used here. At all sweep rates, the films heated to 200 °C have the highest capacity and the capacity decreases by half for films heated to 250 °C. The capacity is nearly lost for films heated to both 300 and 350 °C. Figure 5c shows the charge storage dependence, plotted as capacity versus charging times at all temperatures. The same trend is observed for all temperatures, where the capacity increases with longer charging times, again suggesting V_2O_5 is not fully charged at shorter charging times due to slow diffusion of Li+ ions. In Figure 5c, after a charging time of ≈200 s, the total charge stored at 200 °C is 900 C/g, compared to 600 C/g 250 °C, and ≈200 C/g for both 300 and 350 °C.

To better understand the role of intrinsic kinetic limitations arising from lithium transport in the vanadia layer compared to architectural limitations (pore blocking, electrical conductivity, limited electrolyte diffusion, etc.), we performed CV measurements on flat films of V_2O_5 coated onto flat ITO substrates and heated to the same temperatures (200, 250, 300, and 350 °C). Figure 5b compares the charge storage dependence of flat 7 nm V_2O_5 at sweep rates ranging from 1–100 mV/s. Interestingly, the capacity at all temperatures is less dependent on the sweep rate for flat films in Figure 5b compared to porous films in Figure 5a, suggesting that solvent diffusion through the pore system or electrical conductivity in the porous ITO network may contribute to the kinetic limitations. In

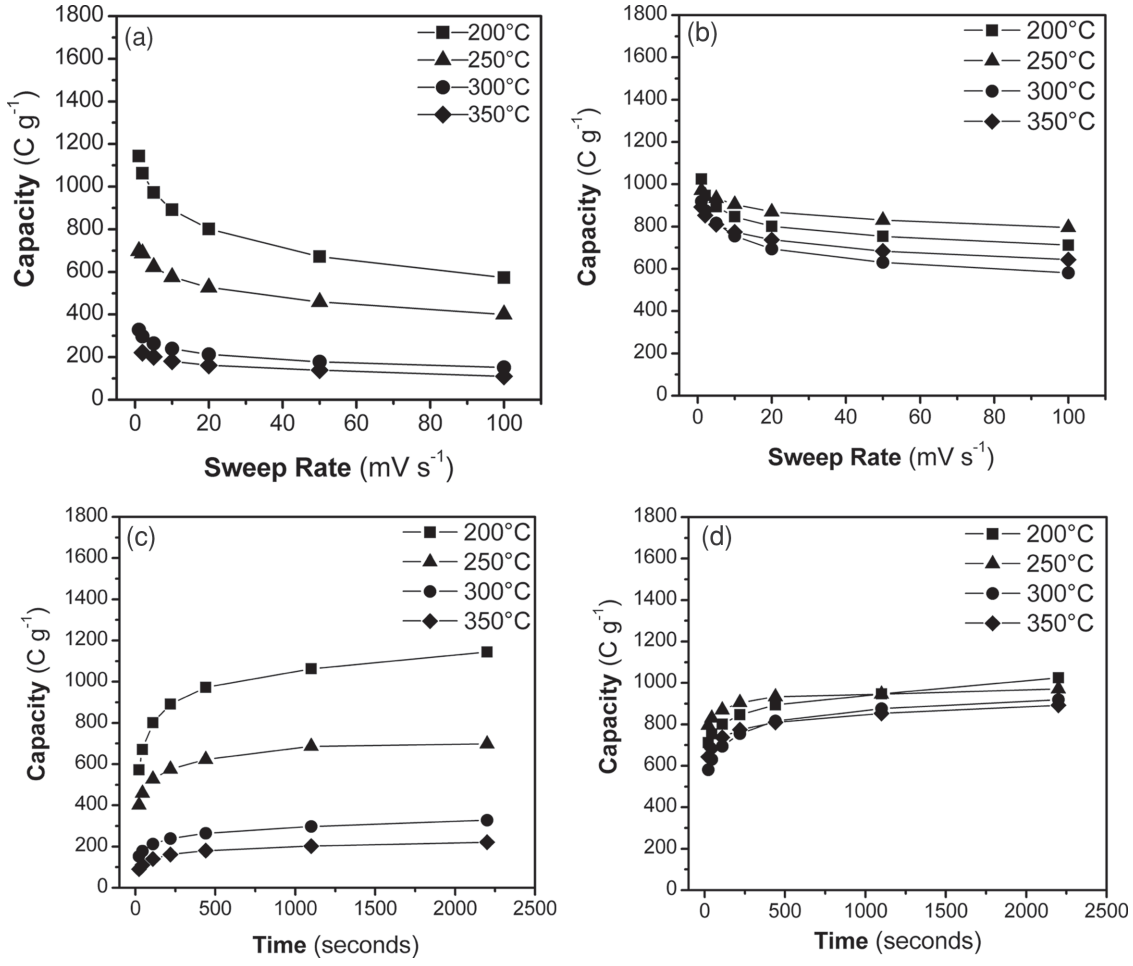

Figure 5. a) Charge storage dependence on sweep rate for mesoporous ITO films coated with a 7 nm layer of V_2O_5 heated to 200, 250, 300 and 350 °C. b) Charge storage dependence on sweep rate for flat ITO coated with a 7 nm layer of V_2O_5 heated to 200, 250, 300, and 350 °C. c) Comparison of charging rates calculated from cyclic voltammetric data at various sweep rates for mesoporous ITO films coated with a 7 nm layer of V_2O_5 heated to 200, 250, 300 and 350 °C. d) Comparison of charging rates calculated from cyclic voltammetric data at various sweep rates for flat ITO coated with a 7 nm layer of V_2O_5 heated to 200, 250, 300, and 350 °C.

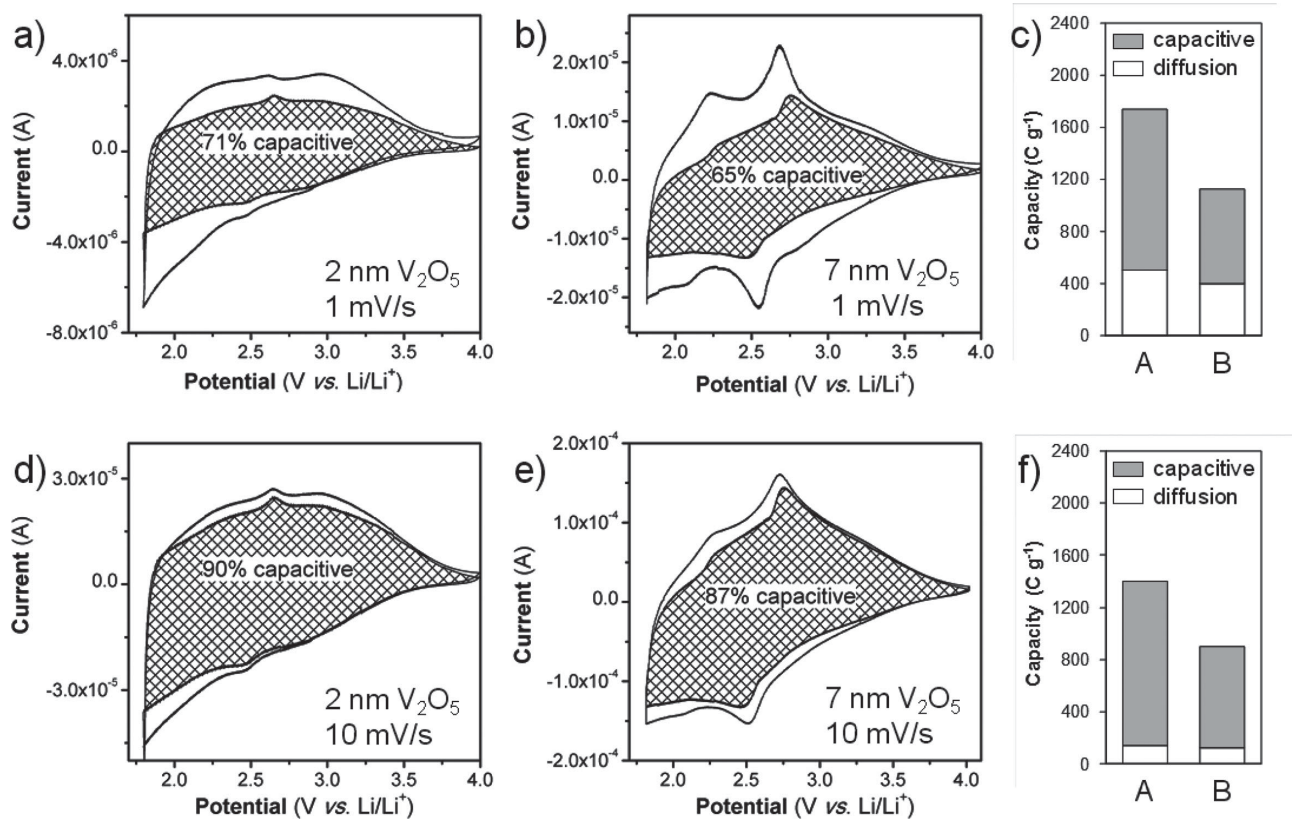

Figure 6. Cyclic voltammetric responses for porous ITO films coated with a) 2 nm and b) 7 nm layer of V_2O_5 heated to 200 °C at sweep rates of 1 mV/s. Cyclic voltammetric responses for the same films, 2 nm (d) and 7 nm (e) layer of V_2O_5, at sweep rates of 10 mV/s. The capacitive contribution to the current is represented as the shaded area. Corresponding comparison of the total stored charge at sweep rates of c) 1 and f) 10 mV/s, where A and B represent 2 and 7 nm layer of V_2O_5 heated to 200 °C.

addition, despite the fact that the films heated to higher temperature are more crystalline, the capacity is similar at all temperatures to within experimental error, a result that makes sense given that grain growth cannot block pores in a flat film. Moreover, none of these films were heated high enough to drive a phase transition to the monoclinic phase. Figure 5d shows the charge storage dependence plotted as capacity versus charging times for the flat V_2O_5 films. At all temperatures, the V_2O_5 is fully charged by ≈200 s, to within experimental error. This suggests the storage of Li+ ions occurs by fast surface redox reactions at all temperatures, and the kinetic limitations in the porous films result from architectural factors. Similar experiments were also performed on 2 nm V_2O_5 layers coated onto flat ITO. Unfortunately, the mass loading for flat 2 nm V_2O_5 layers was too low to obtain meaningful gravimetrically normalized capacity data. While the data is not included here and cannot be discussed in detail, it is worth noting that the general trend in the data was very similar to the trends observed in Figures 5a and b with sample heated to 450 ºC showing about half the capacity of the low temperature samples, likely due to a crystal growth and phase transition to a less redox active phase at high T.

2.4. Pseudocapacitance in ITO-V_2O_5 Composites

As discussed above, pore blocking caused by grain growth can have a significant effect on total capacity measurements. Kinetic studies, which ask what fraction of the total capacity is non-diffusion controlled (and thus capacitive), provide an alternative way to analyze the electrochemical results that is less sensitive to this pore blocking. We thus follow previously reported work to quantitatively determine the capacitive contribution to the current response by using the voltammetric sweep rate dependence of the current.[46] In this analysis, the total current can be separated into two components based on their relationship to the sweep rate of a cyclic voltammetry experiment (ν, in mV/s). One of these components arises from semi-infinite diffusion processes and varies with $\nu^{-1/2}$ and the other is related to capacitive (or surface) processes and varies linearly with ν. Therefore, the current response (i) at a fixed potential (V) can be described as the combination of these two separate mechanisms:

$$i(\mathrm{V}) = \mathrm{k}_1\nu + \mathrm{k}_2\nu^{1/2} \quad (1)$$

where k_1 and k_2 are constants at a particular sweep rate. By determining both k_1 and k_2, we can use the above equation to distinguish between the currents arising from diffusion processes and those from capacitive effects, as previously demonstrated.[40]

Figure 6 shows the total stored charge for mesoporous ITO coated with 2 nm and 7 nm V_2O_5 layers heated to 200 °C at two different sweep rates, 1 and 10 mV/s. The total current or stored charge (total area integrated under the CV curves) is

divided into diffusion-controlled and capacitive (non-diffusion) charge storage. In Figure 6a–b,d–e, the shaded area represents the capacitive current and the white area represents the diffusion-controlled current contributions to the total stored charge. The gravimetrically normalized stored charge, divided into capacitive (shaded area) and diffusion-controlled (white area) contributions, is represented in Figure 6c (1 mV/s) and Figure 6f (10 mV/s).

At a slow sweep rate of 1 mV/s, 2 nm V_2O_5 features a slightly higher diffusion-controlled capacity (≈500 C/g) than 7 nm V_2O_5 (≈400 C/g). This can be explained by the higher porosity observed in 2 nm V_2O_5 (Figure 2c) compared to 7 nm V_2O_5 (Figure 2e), resulting in more accessible redox sites with shorter diffusion path lengths for the electrolyte. In addition, 2 nm V_2O_5 shows a higher amount of total stored charge (≈1700 C/g) compared to 7 nm V_2O_5 (≈1100 C/g), as well as a higher capacitive charge storage (≈1200 C/g) compared to 7 nm V_2O_5 (≈700 C/g). These results suggest that there are more redox sites available for fast charge storage in 2 nm V_2O_5, likely due to a higher surface area resulting from a higher pore volume (Figure 2c). These results also reveal that the surface area loss that is observed in 7 nm V_2O_5, due to grain growth that clogs the smaller pores (Figure 2e, 3e), inhibits capacitive charge storage and impedes diffusion-controlled processes. Despite these differences in total mass normalized capacity, the fraction of the total stored charge that is capacitive in both materials is similar, indicating similar kinetics for diffusion of Li^+ into both thick and thin vanadia layers.

Figure 6f shows the gravimetrically normalized capacities for 2 and 7 nm V_2O_5 cycled at a faster sweep rate (10 mV/s). Since the capacitive charge storage is unaffected by the increase in sweep rate the value is the same as at 1 mV/s for each thickness. This can be explained by the presence of both double-layer and pseudocapacitive processes that are not kinetically limited. By contrast, any slow diffusion of Li+ ions into V_2O_5 is reduced because the Li+ ions have less time to diffuse into the V_2O_5 network. Therefore, the relative capacitive contribution to the total stored charge is greater for both 2 and 7 nm V_2O_5 compared to the contribution from diffusion-controlled mechanisms. Again, both 2 and 7 nm V_2O_5 layers show similar and very high capacitive contributions at 90% and 87%, respectively, of the total stored charge is coming from non-diffusion controlled processes.

All of the data discussed above has been gravimetrically normalized to the total vanadia content, but the samples with 7nm thick vanadia coating obviously contain more vanadia per unit film area. This can be easily seen in the CV curves in Figure 6a–b,d–e, which shows that the total stored charge (area under CV curve, not gravimetrically normalized) is greater for 7 nm V_2O_5 compared to 2 nm V_2O_5. Much less of this vanadia mass is exposed to the electrolyte in the 7 nm thick V_2O_5 samples, however. If we look at the shape of CVs for 2 nm versus 7 nm V_2O_5, there are more defined redox peaks for 7 nm V_2O_5 suggesting the structure is more ordered and feature more specific redox sites in the V_2O_5 lattice. Both of these facts lead us to conclude that the 7 nm thick samples must be storing more charge in the bulk that is pseudocapacitive than samples with 2 nm thick layers (i.e. samples with 7 nm thick layers show higher levels of intercalation pseudocapacitance).[47] Such

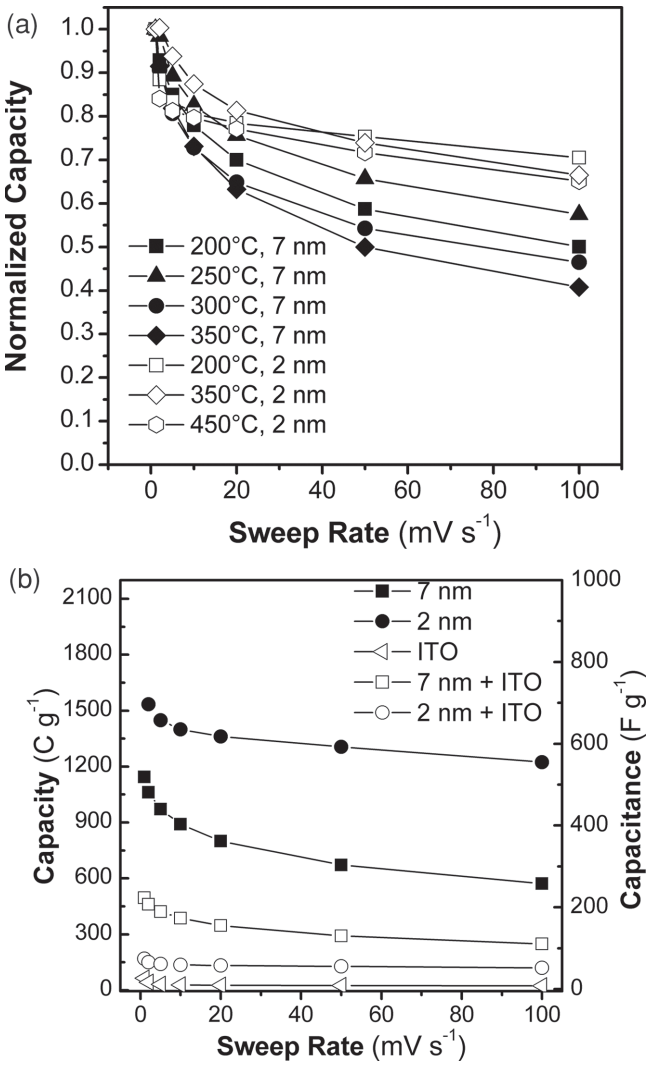

Figure 7. a) Comparison of normalized capacity versus sweep rate calculated from cyclic voltammetric data at various sweep rates for porous ITO coated 2 nm and 7 nm layer of V_2O_5 via ALD heated to various temperatures. b) Comparison of the rate capability of porous ITO coated 2 nm and 7 nm layer of V_2O_5, bare mesoporous ITO, and ITO-V_2O_5 composites including the mass loading for both ITO and V_2O_5.

conclusions are complicated by overall capacity loss in 7 nm thick samples due to pore blocking, however.

To further investigate the rate capability of the ITO-V_2O_5 composites, we thus examine the normalized capacity versus sweep rate for all conditions as shown in **Figure 7**a. For each curve, the capacity is normalized by setting the total stored charge to a value of 1.0 at slow sweep rates. The 2 nm layer heated to 200 °C shows the best rate capability, but the normalized performance is very similar to that obtained for samples with 2 nm V_2O_5 heated to 350 or 450 °C. This result indicates that the number of redox sites may be limited by phase transitions or pore blocking, but the kinetics of all available redox sites are similarly fast. For samples with a 7 nm thick vanadia film, the rate capability is slower in all cases, in agreement with the idea that this sample must show more intercalation pseudocapacitance with longer diffusion lengths. While there is

significant scatter in this data, there is a rough trend that rate capability decreases with increasing temperature, suggesting either that a more crystalline structure leads to slower Li^+ ion diffusion kinetics or that partly blocked pores lead to solution phase barriers for the electrolyte diffusion which add to the solid state barriers for lithium ion diffusion.

Finally, it is important to remember that the ITO conductor is a major component of this system and that ITO has significant mass. Figure 7b compares the charge storage and rate capability of mesoporous ITO coated 2 nm and 7 nm layer of V_2O_5 considering only the vanadia mass, the double layer capacity of the bare mesoporous ITO, and both thick and thin ITO-V_2O_5 composites including the mass for both ITO and V_2O_5. As expected, the bare mesoporous ITO electrode shows very high rate capability but low gravimetrically normalized capacity and capacitance arising only from the electrical double-layer. When the mass of the mesoporous ITO scaffold is included in the calculated gravimetrically normalized capacity and capacitance, as expected, the values decrease significantly since both the 2 nm and 7 nm V_2O_5 layers account for only a small fraction of the total electrode mass. While the 2 nm ITO-V_2O_5 composite shows better rate capability than the 7 nm ITO-V_2O_5 composite, the capacity at all sweep rates is about twice as high for the 7 nm ITO-V_2O_5 composite compared to the 2 nm ITO-V_2O_5, stemming from the fact that the thicker layer has a higher V_2O_5 mass loading.

While the mass normalized capacities that include the ITO mass are not particularly high, it is important to note that this is a not meant to be a commercial battery system, but rather a proof-of-concept exploration of architecture. The mass of ITO, which includes two heavy elements, is anomalously high for a conductor, so its total effect on the mass normalized capacity is disproportionately high. The more important results of this work are an increased understanding of the important factors needed to design a core-shell porous network for pseudocapacitive charge storage. Specifically, we observe pseudocapacitance up to a thickness of 7 nm V_2O_5, which is the limit for our system, as any thicker layer leads to blockage of the pores.

3. Conclusion

In this work, we explored the design of nanoscale pseudocapacitor architecture, constructed using templating of conducting ITO nanocrystals to form a high surface area mesoporous scaffold, followed by coating these porous conductors with a redox-active layer of V_2O_5 to produce nanoporous composites for pseudocapacitive energy storage. By varying the thickness of the V_2O_5 layer as well as the extent of crystallization through various annealing temperatures, the charge storage behavior and rate capability of the composites were examined. Thin V_2O_5 layers (2 nm) feature on open interconnected porosity and a high surface area, leading to charge storage arising primarily from capacitive processes. Thicker layers showed increased capacity on an area normalized basis, but reduced capacity on a mass normalized basis, indicating that electrolyte accessible to some of the pores was blocked.

The crystal structure was also found to play a role in the charge storage behavior in our composites. In general, modest heating to crystallize the V_2O_5 to the orthorhombic phase ($T \leq 350$ °C) led to higher pseudocapacitance. Heating V_2O_5 to temperatures high enough to form the monoclinic phase (>400 °C) led to a decrease in total charge storage and rate capability, again indicating that intercalation pseudocapacitance plays a role, even in samples with 2 nm vanadia films. In thick porous layers, heating V_2O_5 led to significant grain growth that blocked access of the electrolyte to the redox sites, which led to a significant drop in capacity. The capacity of flat V_2O_5 films did not decrease with heating, however, indicating that the reduced capacity in the porous samples with 7 nm thick vanadia layers stemmed from architectural changes upon heating, rather than changes in lithium ion diffusion as the vanadia crystallized.

Taken together, these results provide significant insight on the design of pseudocapacitive materials using a core-shell architecture. Thin shells retain the high surface area of the host conductor and show good kinetics, but the total mass loading of redox active material is not high. Thicker films solve the problem of low mass loading, and if the crystal structure is optimized for Li^+ insertion, near surface redox sites several nm into the material can show fast redox kinetics. Thick films in a core-shell structure can lead to a loss of surface area and pore access, however, and have significant potential for grain growth and structural rearrangement upon thermal processing. Based on our findings, an ideal pseudocapacitor architecture features a high surface area conductor with pores just large enough that they can be coated with an moderately thick layer of active material to form a high surface area core-shell structure that exhibits an open interconnected porosity. By applying these fundamental design rules, it may become possible to build pseudocapacitor materials that will achieve high charge storage while maintaining fast charging/discharging kinetics.

4. Experimental Section

Materials: The following chemicals were purchased and used as received: oleylamine (90% Aldrich), oleic acid (90%, Aldrich), indium acetylacetonate (99.99+%, Aldrich), tin bis(acetylacetonate) dichloride (98%, Aldrich), nitrosonium tetrafluoroborate (95%, Aldrich), Vanadium tri-isopropoxide, (96%, Alfa Aesar). Poly((ethylene-*alt*-propylene)-*block*-poly(ethylene oxide), with a mass ratio of PEP(3900)-*b*-PEO(4000), a block ratio of PEP_{56}-*b*-PEO_{91}, and with a PDI = 1.05, was synthesized using reported methods.[48,49] Briefly, polyisoprene was grown by anionic polymerization, terminated with an -OH group and then hydrogenated over Pd/C. The resulting PEP-OH was subsequently extended by anionic polymerization of ethylene oxide.

Synthesis and Ligand-Exchange of Nanocrystals: Previously reported procedures were followed to synthesize 7–8 nm and 4–5 nm ITO nanocrystals that were stabilized by either oleylamine or oleic acid ligands.[35,36,50] All as-synthesized nanocrystals were purified and dispersed in hexane (10–15 mg/mL). To carry out the ligand-exchange process, as-synthesized nanocrystals were treated with nitrosonium tetrafluoroborate ($NOBF_4$) according to a recently reported procedure.[26] In a typical ligand-exchange reaction, 5 mL of nanocrystal dispersion in hexane was combined with 5 mL of $NOBF_4$ solution in N, N-dimethylformamide (DMF) (10 mg/mL) with stirring (5 min), or until the nanocrystals were transferred to the DMF phase. The nanocrystals were precipitated with toluene then centrifuged, followed by multiple washings with DMF/toluene. The ligand-stripped nanocrystals were dispersed in DMF/ethanol (1:10 v/v) to give a final concentration of 15–20 mg/mL.

Synthesis of Mesoporous Nanocrystal-based Films: The synthesis of mesoporous ITO nanocrystal-based films was previously reported.[30] Briefly, in a typical synthesis, 40 mg of the desired diblock copolymer was dissolved in 0.5 mL of ethanol with gentle heating. To this solution, 3 mL of the desired nanocrystals in DMF/ethanol (20 mg/mL) was added. From this mixture, thin films were produced by dip-coating onto polar substrates at a constant withdrawal rate of 1–10 mm/s with a constant 30% relative humidity. Thin films were also prepared by spin-coating onto polar substrates at 1000 to 2000 rpm for 60 s. The films were dried using a 3 h ramp up to 175 °C, followed by a 3 h soak. Thermal decomposition of the template was done after the drying step using a 6 h ramp from 175 °C to 450 °C, followed by a 3 h soak.

Synthesis of V_2O_5-ITO Composites: The ALD V_2O_5 process was performed in a commercial BENEQ TFS 500 reactor, which has a base pressure of 2 mbar. Vanadium tri-isopropoxide, $VO(OC_3H_7)_3$ (VTOP), was used as the vanadium precursor, which was kept at 45 °C giving a vapor pressure of ≈0.29 torr. Ozone or water was used as the oxidant. O_3 with 18 wt% was generated from pure O_2 source by a MKS O3MEGA ozone delivery system. Ozone ALD was done at 170 °C while water ALD was done at 120 °C. The film thickness was measured ex-situ using a SOPRA GES5 spectroscopic ellipsometer. The 2 and 7 nm V_2O_5 film was done with 100 and 250 ALD cycles respectively. One ALD cycle includes 0.5 s VTOP pulse, 1 s N_2 purge, 2 s oxidant pulse and 1 s N_2 purge. After coated with V_2O_5, the ITO films were post-annealed in oxygen for 60 s using an AG Associates 410 rapid thermal annealer at 200, 250, 300, 350, and 450 °C. The thickness of the films is estimated based on the number of ALD cycles.

Methods: The mass of the V_2O_5 composites was determined by inductively coupled plasma optical emission spectroscopy (ICP-OES), performed on a TJA RADIAL IRIS 1000. Transmission electron microscopy (TEM) images were obtained using an FEI/PHILIPS CM120 electron microscope operating at 120 kV. Scanning electron microscopy (SEM) images were obtained using a JEOL model 6700F electron microscope with beam energy 5 kV. 2D small-angle X-ray scattering (2D-SAXS) data were collected at the Stanford Synchrotron Radiation Laboratory using beamline 1–4 using the Rayonix165 large angle CCD detector. All measurements were performed in reflection geometry. XPS analysis was performed using a Kratos Axis Ultra DLD with a monochromatic (Kα radiation) source. The charge neutralizer filament was used to control charging of the sample. A 20 eV pass energy was used with a 0.05 eV pass energy. Scans were calibrated using the C 1s peak shifted to 284.8 eV. Ellipsometric porosimetry was performed on a PS-1000 instrument from Semilab using toluene as the adsorbate. A UV–visible CCD detector adapted to a grating spectrograph analyzes the signal reflected by the sample. The light source is a 75 W Hamamatsu Xenon lamp and measurements were performed on the spectral range from 1.24–4.5 eV. Data analysis was performed using the associated SEA software with the assumption of slit-like pores. If the actual pores are closer to cylindrical, the real pores sizes will be slightly larger than the values reported here. Data is fit with a contact angle of zero for the solvent. Electrochemical measurements were carried out in a three-electrode cell using a PAR EG&G 273A potentiostat in an argon-filled glovebox, with oxygen and water levels <1 ppm. The working electrode consisted of ITO glass upon which ITO-V_2O_5 films were deposited. The electrolyte solution used was 1.0 M $LiClO_4$ in propylene carbonate (PC) and lithium metal foils were used as the counter and reference electrodes. Cyclic voltammetry was performed using cutoff voltages at 4 and 1.8 V vs Li/Li^+.

Supporting Information

Supporting Information is available from the Wiley Online Library or from the author.

Acknowledgements

The authors would like to thank Dr. Morgan Stefik and Prof. Ulrich Wiesner (Cornell University, Materials Science and Engineering) for synthesizing the PEP-PEO diblock copolymer used in this work. The authors would also like to thank Dr. Raffaella Buonsanti and Dr. Delia J. Milliron (Molecular Foundry, Lawrence Berkeley National Laboratory), for the synthesis of ITO nanocrystals. This work was supported by the center for Molecularly Engineered Energy Materials (MEEM), an Energy Frontier Research Center funded by the US Department of Energy (D.O.E.), Office of Science, Office of Basic Energy Sciences under Award Number DE-SC0001342. (I. Rauda, V. Augustyn, L.C. Saldarriaga-Lopez, L. Schelhas, B. Dunn, S. H. Tolbert, synthesis of porous ITO, SEM, porosimetry, TEM, electrochemistry, and kinetic studies) and by the center for Nanostructures for Electrical Energy Storage (NEES), an Energy Frontier Research Center funded by the U.S. Department of Energy, Office of Science, Office of Basic Energy Sciences, under Award Number DESC0001160. (X. Chen and G.W. Rubloff, ALD development, depositions, and annealing). This work made use of XPS facility at the department of chemistry and biochemistry at UCLA acquired under NSF Award CHE-0840531. The authors acknowledge the use of instruments at the Electron Imaging Center for NanoMachines supported by NIH (1S10RR23057 to ZHZ) at the California NanoSystems Institute, UCLA.

Received: April 21, 2014
Revised: July 7, 2014
Published online: September 1, 2014

[1] B. E. Conway, W. G. Pell, *J. Solid State Electrochem.* **2003**, *7*, 637–644.
[2] J. R. Miller, P. Simon, *Science* **2008**, *321*, 651–652.
[3] K.-W. Nam, C.-W. Lee, X.-Q. Yang, B. W. Cho, W.-S. Yoon, K.-B. Kim, *J. Power Sources* **2009**, *188*, 323–331.
[4] A. L. M. Reddy, S. Ramaprabhu, *J. Phys. Chem. C* **2007**, *111*, 7727–7734.
[5] X. Zhao, C. M. Hayner, H. H. Kung, *J. Mater. Chem.* **2011**, *21*, 17297–17303.
[6] M. Sathiya, A. S. Prakash, K. Ramesha, J.-M. Tarascon, A. K. Shukla, *J. Am. Chem. Soc.* **2011**, *133*, 16291–16299.
[7] Z. Chen, V. Augustyn, J. Wen, Y. Zhang, M. Shen, B. Dunn, Y. Lu, *Adv. Mater.* **2011**, *23*, 791–795.
[8] I.-H. Kim, J.-H. Kim, B.-W. Cho, K.-B. Kim, *J. Electrochem. Soc.* **2006**, *153*, A1451–A1458.
[9] J. S. Sakamoto, B. Dunn, *J. Electrochem. Soc.* **2002**, *149*, A26–A30
[10] X. Chen, H. Zhu, Y-C. Chen, Y. Shang, A. Cao, L. Hu, G. W. Rubloff, *ACS Nano* **2012**, *6*, 7948–7955.
[11] W. Chen, S. Li, C. Chen, L. Yan, *Adv. Mater.* **2011**, *23*, 5679–5683.
[12] D. Wang, R. Kou, D. Choi, Z. Yang, Z. Nie, J. Li, L. V. Saraf, D. Hu, J. Zhang, G. L. Graff, J. Liu, M. A. Pope, I. A. Aksay, *ACS Nano* **2010**, *4*, 1587–1595.
[13] H. Wang, H. S. Casalongue, Y. Liang, H. Dai, *J. Am. Chem. Soc.* **2010**, *132*, 7472–7477.
[14] G. Yu, L. Hu, N. Liu, H. Wang, M. Vosgueritchian, Y. Yang, Y. Cui, Z. Bao, *Nano Lett.* **2011**, *11*, 4438–4442.
[15] J. C. Lytle, J. M. Wallace, M. B. Sassin, A. J. Barrow, J. W. Long, J. L. Dysart, C. H. Renninger, M. P. Saunders, N. L. Brandell, D. R. Rolison, *Energy Environ. Sci.* **2011**, *4*, 1913–1925.
[16] J. W. Long, D. R. Rolison, *Acc. Chem. Res.* **2007**, *40*, 854–862.
[17] H. Zhang, X. Yu, P. V. Braun, *Nat. Nanotechnol.* **2011**, *6*, 277–281.
[18] X. Lang, A. Hirata, T. Fujita, M. Chen, *Nat. Nanotechnol.* **2011**, *6*, 232–236.
[19] J. Li, Q. M. Yang, I. Zhitomirsky, *J. Power Sources* **2008**, *185*, 1569–1574.
[20] J. R. McDonough, J. W. Choi, Y. Yang, F. La Mantia, Y. Zhang, Y. Cui, *Appl. Phys. Lett.* **2009**, *95*, 243109(1–3).
[21] P. L. Taberna, S. Mitra, P. Poizot, P. Simon, J.-M. Tarascon, *Nat. Mater.* **2006**, *5*, 567–573.
[22] J.-H. Kim, S.-T. Myung, Y.-K. Sun, *Electrochem. Acta* **2004**, *49*, 219–227.

[23] T. Brezesinski, J. Wang, J. Polleux, B. Dunn, S. H. Tolbert, *J. Am. Chem. Soc.* **2009**, *131*, 1802–1809.
[24] J. M. Szeifert, J. M. Feckl, D. Fattakhova-Rohlfing, Y. Liu, V. Kalousek, J. Rathousky, T. Bein, *J. Am. Chem. Soc.* **2010**, *132*, 12605–12611.
[25] S. C. Warren, L. C. Messina, L. S. Slaughter, M. Kamperman, Q. Zhou, S. M. Gruner, F. J. DiSalvo, U. Wiesner, *Science* **2008**, *320*, 1748–1752.
[26] A. Corma, P. Atienzar, H. Garcia, J. Y. Chane-Ching, *Nat. Mater.* **2004**, *3*, 394–397.
[27] A. S. Deshpande, N. Pinna, B. Smarsly, M. Antonietti, M. Niederberger, *Small* **2005**, *1*, 313–316.
[28] J. Ba, J. Polleux, M. Antonietti, M. Niederberger, *Adv. Mater.* **2005**, *17*, 2509–2512.
[29] A. Dong, X. Ye, J. Chen, Y. Kang, T. Gordon, J. M. Kikkawa, C. B. Murray, *J. Am. Chem. Soc.* **2011**, *133*, 998–1006.
[30] I. E. Rauda, R. Buonsanti, L. C. Saldarriaga-Lopez, K. Benjauthrit, L. T. Schelhas, M. Stefik, V. Augustyn, J. Ko, B. Dunn, U. Wiesner, D. J. Milliron, S. H. Tolbert, *ACS Nano* **2012**, *6*, 6386–6399.
[31] I. E. Rauda, L. C. Saldarriaga-Lopez, B. A. Helms, L. T. Schelhas, D. Membreno, D. J. Milliron, S. H. Tolbert, *Adv. Mater.* **2013**, *25*, 1315–1322.
[32] R. Buonsanti, T. E. Pick, N. Krins, T. J. Richardson, B. A. Helms, D. J. Milliron, *Nano Lett.* **2012**, *12*, 3872–3877.
[33] X. Chen, E. Pomerantseva, P. Banerjee, K. Gregorczyk, R. Ghodssi, G. Rubloff, *Chem. Mater.* **2012**, *24*, 1255–1261.
[34] X. Chen, E. Pomerantseva, K. Gregorczyk, R. Ghodssi, G. Rubloff, *RSC Adv.* **2013**, *3*, 4294–4302.
[35] R. A. Giltsrap Jr., C. J. Capozzi, C. G. Carson, R. A. Gerhardt, C. J. Summers, *Adv. Mater.* **2008**, *20*, 4163–4166.
[36] S. I. Choi, K. M. Nam, B. K. Park, W. S. Seo, J. T. Park, *Chem. Mater.* **2008**, *20*, 2609–2611.
[37] Y. Lu, R. Ganguli, C. A. Drewien, M. T. Anderson, C. J. Brinker, W. Gong, Y. Guo, H. Soyez, B. Dunn, M. H. Huang, J. I. Zink, *Nature* **1997**, *389*, 364–368.
[38] M. R. Baklanov, K. P. Mogilnikov, V. G. Polovinkin, F. N. Dultsev, *J. of Vac. Sci. & Tech. B* **2000**, *18*, 1385–1391.
[39] S. J. Gregg, K. S. W. Sing, *Adsorption, Surface Area, and Porosity*, 2nd ed., Academic, London **1982**.
[40] S. M. George, *Chem. Rev.* **2010**, *110*, 111–131.
[41] J. W. Elam, G. Xiong, C. Y. Han, H. Hau Wang, J. P. Birrell, U. Welp, J. N. Hryn, M. J. Pellin, T. F. Baumann, J. F. Poco, J. H. Satcher Jr, *J. Nanomater.* **2006**, 1–5.
[42] G. Silversmit, D. Depla, H. Poelman, G. Marin, R. De Gryse, *J. Electron. Spectrosc. Relat. Phenom.* **2004**, *135*, 167–175.
[43] J. Livage, *Chem. Mater.* **1991**, *3*, 578–593.
[44] Y. Wang, K. Takahashi, K. H. Lee, G. Z. Cao, *Adv. Funct. Mater.* **2006**, *16*, 1133–1144.
[45] A. Talledo, H. Valdivia, C. Benndorf J. Vac. Sci. Technol. A *J. Vac. Sci. Technol. A* **2003**, *21*, 1494–1499.
[46] T.-C. Liu, W. G. Pell, B. E. Conway, S. L. Roberson. *J. Electrochem. Soc.* **1998**, *145*, 1882–1888.
[47] V. Augustyn, J. Come, M. A. Lowe, J. W. Kim, P.-L. Taberna, S. H. Tolbert, H. D. Abruña, P. Simon, B. Dunn, *Nat. Mater.* **2013**, *12*, 518–522.
[48] M. A. Hillmyer, F. S. Bates, *Macromolecules* **1996**, *29*, 6994–7002.
[49] J. Allgaier, A. Poppe, L. Willner, D. Richter, *Macromolecules* **1997**, *30*, 1582–1586.
[50] A. Llordes, A. T. Hammack, R. Buonsanti, R. Tangirala, S. Aloni, B. A. Helms, D. J. Milliron, *J. Mater. Chem.* **2011**, *21*, 11631–11638.